random SL films were 20 to 60% when prepared from the *t*-TPA gel and below 12% when prepared from the TPA gel.

Another major application of zeolite films is in membrane-mediated separation of small-molecule mixtures into pure components. The separation of xylenes has received particular attention (*4*, *8*). To investigate the performance of uniformly *b*-oriented SL films as xylene mixture-separation membranes, we prepared monolayers of rounded coffin-shaped SL crystals on porous silica supports and subsequently grew 1.0-μm-thick uniformly *b*-oriented SL films (fig. S24) in gel-2 (SOM methods). The use of porous silica supports is necessary to maintain uniform *b*-orientation of the SL films, because aluminum-containing porous supports suppress the film growth. The preparation of the porous silica supports was readily achieved by one step: 2 hours of calcination at 1020°C (SOM methods). The separation of the *o*- and *p*-xylene mixture was conducted at two different temperatures (80° and 150°C) under standard reported conditions (SOM methods and fig. S25).

The initially measured permeance of *p*-xylene at 80°C was much higher than that of *o*-xylene, giving rise to a high (>1900) separation factor (SF) (Fig. 4D). However, the permeances continuously decreased over a period of 216 hours and reached a steady state. The steady-state permeances of *p*-xylene and *o*-xylene were 0.7×10^{-8} and 0.0092×10^{-8} mol s^{-1} m^{-2} Pa^{-1}, respectively, giving rise to a steady-state SF of 71. We attribute the continuous decreases of *p*-xylene permeance and the SF value to gradual adsorption of *o*-xylene into the channels, leading to a gradual increase in the degree of channel blockage, which in turn decreases the diffusion rate of *p*-xylene molecules (*11*). The fact that the permeance decreases to near zero also indicates that the *b*-oriented SL film does not have cracks.

At 150°C, the *p*-xylene permeance also continuously decreased from 21.6×10^{-8} to 5×10^{-8} mol s^{-1} m^{-2} Pa^{-1} over a period of 400 hours (Fig. 4E). During the same period, the *o*-xylene permeance decreased from 0.0097×10^{-8} to 0.0068×10^{-8} mol s^{-1} m^{-2} Pa^{-1}. The gradual decrease of *p*-xylene permeance even at 150°C indicates that the channel blocking by *o*-xylene still continues at 150°C, and the *b*-oriented SL film does not undergo crack formation during the operation. During the period from 20 to 370 hours, the SF value remained nearly constant at ~1000. Although this steady-state SF value is lower than the highest value observed from randomly oriented tubular SL films (*12*), it is about two times higher than those of randomly oriented non-tubular SL films with similar thickness (table S5).

We have reported straightforward methods to prepare uniformly *a*- and *b*-oriented SL films and *a*-oriented Si-BEA films. The control of orientation is not limited to the channel upright directions but can be applied to any desired directions by finding proper methods to uniformly orient SL and Si-BEA crystals in those directions on supports. We believe our findings will trigger extensions of the methods to the preparation of various other types of zeolite films in perfectly uniform orientations.

References and Notes

1. J. O'Brien-Abraham, J. Y. S. Lin, in *Zeolites in Industrial Separation and Catalysis*, S. Kulprathipanja, Ed. (Wiley VCH, Verlag, Weinheim, Germany, 2010), chap. 3, pp. 307–329.
2. J. Caro, M. Noack, in *Advances in Nanoporous Materials*, S. Ernst, Ed. (Elsevier, Amsterdam, 2009), vol. 1, chap. 1, pp. 1–96.
3. J. Caro, M. Noack, *Microporous Mesoporous Mater.* **115**, 215 (2008).
4. J. Choi *et al.*, *Science* **325**, 590 (2009).
5. J. Hedlund, F. Jareman, A. J. Bons, M. Anthonis, *J. Membr. Sci.* **222**, 163 (2003).
6. Z. P. Lai, M. Tsapatsis, J. R. Nicolich, *Adv. Funct. Mater.* **14**, 716 (2004).
7. C. J. Gump, V. A. Tuan, R. D. Noble, J. L. Falconer, *Ind. Eng. Chem. Res.* **40**, 565 (2001).
8. Z. P. Lai *et al.*, *Science* **300**, 456 (2003).
9. M. A. Snyder, M. Tsapatsis, *Angew. Chem. Int. Ed.* **46**, 7560 (2007).
10. H. H. Funke, A. M. Argo, J. L. Falconer, R. D. Noble, *Ind. Eng. Chem. Res.* **36**, 137 (1997).
11. J. O'Brien-Abraham, M. Kanezashi, Y. S. Lin, *J. Membr. Sci.* **320**, 505 (2008).
12. M. O. Daramola *et al.*, *Sep. Sci. Technol.* **45**, 21 (2009).
13. H. Guo *et al.*, *Angew. Chem. Int. Ed.* **45**, 7053 (2006).
14. H. S. Kim *et al.*, *J. Am. Chem. Soc.* **126**, 673 (2004).
15. H. S. Kim *et al.*, *Adv. Mater.* **19**, 260 (2007).
16. H. S. Kim, T. T. Pham, K. B. Yoon, *J. Am. Chem. Soc.* **130**, 2131 (2008).
17. C. M. Lew, R. Cai, Y. Yan, *Acc. Chem. Res.* **43**, 210 (2010).
18. Z. Li *et al.*, *Angew. Chem. Int. Ed.* **45**, 6329 (2006).
19. M. E. Davis, *Nature* **417**, 813 (2002).
20. T. Bein, *Chem. Mater.* **8**, 1636 (1996).
21. Y. Liu, Y. S. Li, W. S. Yang, *J. Am. Chem. Soc.* **132**, 1768 (2010).
22. X. Li, Y. Peng, Z. Wang, Y. Yan, *CrystEngComm* **13**, 3657 (2011).
23. MFI and BEA are two different framework-type codes assigned by the Structural Commission of the International Zeolite Association. Silicalite-1 and ZSM-5 belong to MFI. ZSM-5 has aluminosilicate frameworks with varying Si/Al ratios, whereas silicalite-1 has a pure silica framework. BEA is also often called beta zeolite. BEA has aluminosilicate frameworks with varying Si/Al ratios, whereas pure silica BEA (Si-BEA) has a pure silica framework.
24. C. Baerlocher, W. M. Meier, D. H. Olson, *Atlas of Zeolite Framework Types* (Elsevier, Amsterdam, ed. 5, 2001), pp. 184–185.
25. O. Larlus, V. Valtchev, *Microporous Mesoporous Mater.* **93**, 55 (2006).
26. O. Larlus, V. Valtchev, *Chem. Mater.* **17**, 881 (2005).
27. A. Mitra *et al.*, *Ind. Eng. Chem. Res.* **43**, 2946 (2004).
28. A. Mitra *et al.*, *J. Electrochem. Soc.* **149**, B472 (2002).
29. S. Mintova, M. Reinelt, T. H. Metzger, J. Senker, T. Bein, *Chem. Commun.* **2003**, 326 (2003).
30. K. B. Yoon, *Acc. Chem. Res.* **40**, 29 (2007).
31. R. Singh, P. K. Dutta, in *Handbook of Zeolite Science and Technology*, S. Auerbach, K. Carrado, P. Dutta, Eds. (Marcel Dekker, New York, 2003), chap. 2.
32. A. Marinkovic *et al.*, *Microporous Mesoporous Mater.* **71**, 117 (2004).
33. D. Bhange, V. Ramaswamy, *Mater. Res. Bull.* **41**, 1392 (2006).
34. J. S. Lee, J. H. Kim, Y. J. Lee, N. C. Jeong, K. B. Yoon, *Angew. Chem. Int. Ed.* **46**, 3087 (2007).
35. The transfer of nutrients from the dry gel to the seed layer seems to be carried out by a small amount of moisture, which vaporizes into steam at the reaction temperature.
36. As the reaction temperature increases, the growth rate increases. However, as a possible means to incorporate more second-order NLO dyes into the channels, we chose the relatively low reaction temperatures (140° to 180°C) with the hypothesis that the number of defect sites in the channels would decrease as the growth rate decreased.
37. The thickness of the seed crystal does not affect the growth rate. However, if one wants to reach the desired thickness faster, it will be beneficial to start with thicker seed crystals.
38. H. Karsli, A. Çulfaz, H. Yücel, *Zeolites* **12**, 728 (1992).

Acknowledgments: This work was supported by the Korea Center for Artificial Photosynthesis, located at Sogang University and funded by the Ministry of Education of Science and Technology through the National Research Foundation of Korea (NRFK) (grant NRF-2009-C1AAA001-2009-0093879) and the acceleration program of the NRFK. We thank J. Y. Lee for help in drawing Fig. 1. Sogang University has filed patents on the results presented here.

Supporting Online Material

www.sciencemag.org/cgi/content/full/334/6062/1533/DC1
Materials and Methods
SOM Text
Figs. S1 to S25
Tables S1 to S5
References (*39*–*42*)

10 August 2011; accepted 8 November 2011
10.1126/science.1212472

Revealing Atom-Radical Reactivity at Low Temperature Through the N + OH Reaction

Julien Daranlot,[1] Mohamed Jorfi,[2] Changjian Xie,[3] Astrid Bergeat,[1] Michel Costes,[1] Philippe Caubet,[1] Daiqian Xie,[3] Hua Guo,[4] Pascal Honvault,[5,6] Kevin M. Hickson[1]*

More than 100 reactions between stable molecules and free radicals have been shown to remain rapid at low temperatures. In contrast, reactions between two unstable radicals have received much less attention due to the added complexity of producing and measuring excess radical concentrations. We performed kinetic experiments on the barrierless $N(^4S) + OH(^2\Pi) \rightarrow H(^2S) + NO(^2\Pi)$ reaction in a supersonic flow (Laval nozzle) reactor. We used a microwave-discharge method to generate atomic nitrogen and a relative-rate method to follow the reaction kinetics. The measured rates agreed well with the results of exact and approximate quantum mechanical calculations. These results also provide insight into the gas-phase formation mechanisms of molecular nitrogen in interstellar clouds.

The chemistry of low-temperature environments, such as interstellar clouds (ISCs), was thought to be governed by reactions involving electrically charged species (*1*) until recent advances in experimental and theoretical methods showed that reactions between uncharged species could occur and even dominate in some low-temperatures regions. The 1990s

saw the emergence of the CRESU technique (*2*) that applies Laval nozzle expansions to cool gases isentropically while avoiding the wall-loss effects incurred in conventional cryogenic systems. This method has been used to measure the rates for numerous reactions between neutral species at temperatures as low as 6 K (*3*), although only one of them was between two unstable radicals (*4*). Several challenges face experimentalists studying radical-radical kinetics: (i) Can sufficiently large quantities of one of the radical species be generated such that its concentration satisfies the requirements for pseudo–first-order kinetics? (ii) Can this reagent concentration be quantified to extract the thermal rate constant? (iii) Can the method be applied universally to investigate an extensive range of radical-radical reactions?

The only radical-radical reaction to have been studied with the CRESU technique below 100 K is the $O(^3P) + OH(^2\Pi) \rightarrow H(^2S) + O_2(^3\Sigma_g^-)$ reaction (*4*). Excess atomic oxygen was produced by pulsed-laser photolysis (PLP) of O_2 at 157 nm, whereas the decay of OH radicals was followed by laser-induced fluorescence (LIF). The atomic oxygen concentration was estimated from the absorption cross section of O_2 at 157 nm and the laser fluence. Similar schemes can neither produce atomic hydrogen or nitrogen from their molecular counterparts nor estimate their concentrations due to negligible absorption at vacuum ultraviolet wavelengths for both H_2 and N_2.

Given the limited application of PLP methods in this respect, we have applied the microwave-discharge technique as an alternative for the production of atomic species. This method has been used in the gas-phase chemical kinetics community since the 1960s to generate large concentrations of a wide range of atomic species, but it has proven difficult to couple this technique to either continuous or pulsed CRESU apparatuses. The large reservoir volumes and high gas flows used by other continuous CRESU systems mean that the reactive atoms have ample time to recombine and are highly diluted. In pulsed apparatuses, it is difficult to pulse the discharge in a stable manner. The continuous CRESU apparatus used in this study overcomes such issues through reduced gas flows, typically five times lower than other continuous CRESU systems, that are comparable to those used in conventional flow-tube apparatuses. Atoms created upstream of the Laval nozzle yield high densities (10^{14} to 10^{15} cm^{-3}) in the downstream cold supersonic flow, thereby allowing atom-radical reactions with rate constants greater than 5×10^{-12} cm^3 s^{-1} to be studied.

Arguably, the more challenging problem in radical-radical kinetics is the determination of the excess reagent concentration. In kinetics experiments where the excess reagent is a stable molecule, this quantity is obtained directly from its partial pressure, but when the excess reagent is a radical, its production efficiency is poorly known and losses occur both heterogeneously and homogeneously, so a similar analysis for atoms becomes hazardous. Instead, we used an established technique, the relative-rate method, in which the unknown rate of a target reaction is measured relative to the known rate of a reference reaction, the two reactions sharing a common reagent species that is present in excess. The ratio of the pseudo–first-order losses of the two minor reagent species yields the ratio of the rate constants for these processes, provided that secondary reactions do not consume or produce more than a few percent of the minor reagent species. No knowledge of the excess radical reagent concentration is required, but uncertainties arising from the measurement of the reference process must be incorporated into the unknown rate.

To test these methods, we measured rate constants for the important interstellar reaction

$$N(^4S) + OH(^2\Pi) \rightarrow NO(^2\Pi) + H(^2S) \quad (1)$$

relative to that of a previously determined reference reaction (*5*)

$$N(^4S) + NO(^2\Pi) \rightarrow N_2(^1\Sigma_g^+) + O(^3P) \quad (2)$$

Reaction 1 could be the major source of NO in dense ISCs and, in conjunction with reaction 2, mediates the transformation from atomic to molecular

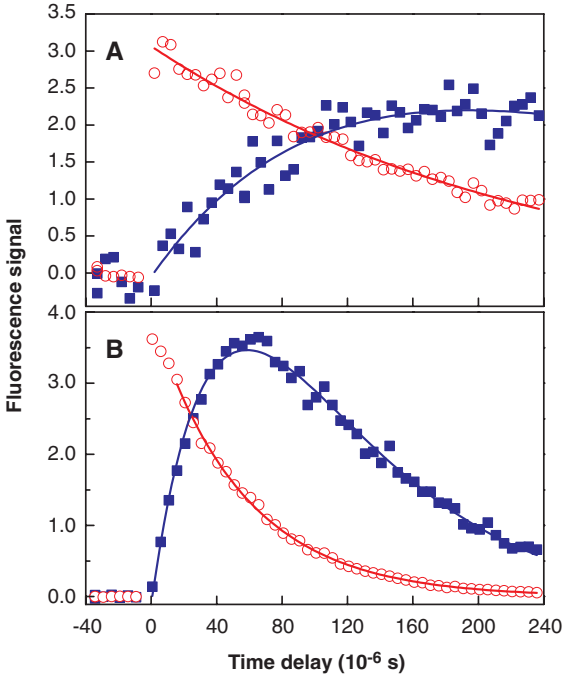

Fig. 1. (**A**) Exemplary temporal profiles at 147 K with estimated [N] = 1.1×10^{14} atoms cm^{-3}. Blue squares, NO($^2\Pi_{1/2}$) LIF signal; red circles, OH($^2\Pi_{3/2}$) LIF signal. (**B**) As in (A) but with estimated [N] = 4.1×10^{14} atoms cm^{-3}.

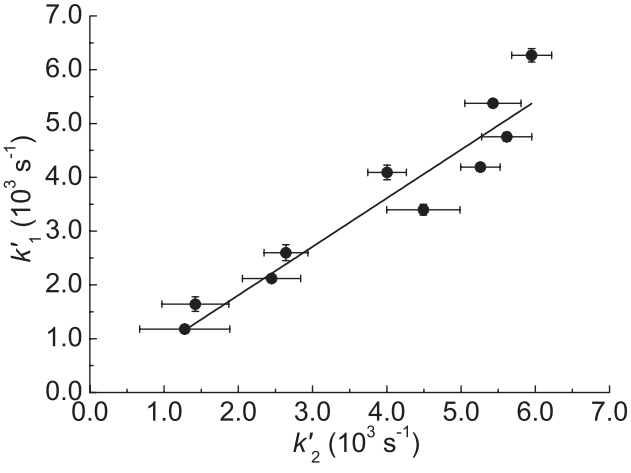

Fig. 2. Pseudo–first-order rate constants for reaction 1 as a function of the pseudo–first-order rate constants for reaction 2 at 56 K. A weighted linear least-squares fit yields the ratio of the second-order rate constants k_1/k_2. The vertical error bars reflect the statistical uncertainties at the level of a single standard deviation obtained by fitting to OH LIF profiles such as those shown in Fig. 1. The horizontal error bars were obtained in the same manner by fitting to the NO LIF profiles.

[1]Université de Bordeaux, Institut des Sciences Moléculaires, CNRS UMR 5255, F-33400 Talence, France. [2]Laboratoire de Catalyse en Chimie Organique, UMR CNRS 6503, Université de Poitiers, 86022 Poitiers Cedex, France. [3]Institute of Theoretical and Computational Chemistry, Key Laboratory of Mesoscopic Chemistry, School of Chemistry and Chemical Engineering, Nanjing University, Nanjing 210093, China. [4]Department of Chemistry and Chemical Biology, University of New Mexico, Albuquerque, NM 87131, USA. [5]Laboratoire Interdisciplinaire Carnot de Bourgogne, UMR CNRS 5209, Université de Bourgogne, 21078 Dijon Cedex, France. [6]UFR Sciences et Techniques, Université de Franche-Comté, 25030 Besançon Cedex, France.

*To whom correspondence should be addressed. E-mail: km.hickson@ism.u-bordeaux1.fr

nitrogen. As the fifth most abundant element in the universe, nitrogen had been thought to occur mostly in the form of N_2 in these regions. N_2 is difficult to observe, however, given the absence of allowed vibrational and/or rotational transitions, so its abundance has been inferred through observations of N_2H^+. These observations show that the atomic-to-molecular nitrogen abundance ratio, N/N_2, in such environments is too high to be compatible with current gas-phase formation mechanisms (*6*). Recommended rate constants for reaction 1 (*7*, *8*) are based on earlier measurements using a cryogenic cooling method (*9*) with a negative temperature dependence ($T^{-0.2}$) for the rate down to 103 K. Recent calculations (*10*–*12*) have brought the validity of these measurements into question, suggesting that reaction 1 may present a less pronounced variation with temperature yielding substantially smaller rate constants at low temperatures. If the rate for reaction 1 is slower than currently predicted, it may present a bottleneck to N_2 formation in dark clouds, thereby bringing models more into line with observations.

We performed experiments in our continuous-flow CRESU apparatus between 56 and 296 K (*13*) [also see supporting online material (*14*)]. Excess concentrations of $N(^4S)$ atoms were produced by microwave discharge upstream of the Laval nozzle, and OH radicals were created in situ by PLP of H_2O_2 vapor. We followed [OH] by LIF to measure the pseudo–first-order rate constant k_1'. Simultaneously, NO molecules produced and consumed by reactions 1 and 2, respectively, were also followed by LIF, yielding kinetic traces similar to those shown in Fig. 1. Under conditions where the formation and loss of NO were governed solely through these two reactions, the temporal evolution of NO was given by

$$[\mathrm{NO}] = \frac{k_1'[\mathrm{OH}]_0}{k_2' - k_1'}(e^{-k_1't} - e^{-k_2't}) \quad (3)$$

where k_2' is the pseudo–first-order rate constant for reaction 2, $[\mathrm{OH}]_0$ and [NO] are the initial OH and time-dependent NO concentrations, respectively, and t is time. The value of k_1' previously obtained was reinserted into Eq. 3 as a constant, and k_2' was varied until a best fit to the data was obtained. Values of k_1' were then plotted as a function of the corresponding k_2' value for different atomic nitrogen concentrations (Fig. 2) to yield the rate constant ratio $k_1'/k_2' \equiv k_1/k_2$ at a specified temperature from the slope. The second-order rate constant k_1 follows from the product of the ratio and the previously measured k_2 values (*5*). Values of k_1 obtained in this manner are listed in table S1 (*14*) and are given as a function of temperature in Fig. 3 alongside earlier experimental and theoretical results.

To check the rate constants obtained for reaction 1 and the validity of the experimental method, we used two quantum mechanical approaches to calculate the rate constants with a high-quality potential energy surface of the a^3A'' state (the lowest triplet electronic state of HNO) developed recently (*12*). First, we used a time-independent quantum mechanical (TIQM) method employing body-frame hyperspherical coordinates (*15*). At each hyperradius ρ, a set of reference Hamiltonian eigenstates was calculated. At small ρ, the adiabatic states in each sector spanned a large fraction of configuration space, allowing for atom exchange. These states were expanded on a basis of pseudo-hyperspherical harmonics with appropriate symmetries, dissociating at large ρ into various NO and OH rovibrational sets. The expansion coefficients satisfied a set of second-order coupled differential equations with couplings arising from the difference between exact and reference Hamiltonians. The range of variation of ρ was divided into 147 equal sectors between 2.9 and 21.1 bohr. The crucial parameters for convergence were the number of states included and the asymptotic matching distance, both of which we checked carefully. All TIQM calculations were performed for N + OH ($v = 0$, $j = 0$) → NO + H (that is, OH in its ground rovibrational state) (where v and j are the vibrational and rotational quantum numbers, respectively). Once the accurate total reaction probability had been computed for a total angular momentum $J = 0$, the rate constant was obtained by the J-shifting approach (*16*) from 10 to 350 K. Higher vibrational states of OH were not considered, as excited states are unpopulated below 350 K. In addition, recent quasi-classical trajectory studies (*11*) down to 5 K show that the rate constant is relatively insensitive to the OH rotational state, as the rate constant calculated for $v = 0$, $j = 0$ approaches the thermal rate.

Second, we performed exact time-dependent quantum mechanical (TDQM) calculations including contributions from all angular momenta J in the N + OH Jacobi coordinates. A Gaussian wave packet with the ground rovibrational state OH reactant was launched in the N + OH channel and propagated in time with the split-operator method. The wave packet was discretized in a mixed representation in which the radial coordinates were represented in grids and angular coordinates in basis functions; the S-matrix elements were obtained by projecting the wave packet to the product basis (*17*). We calculated the total reaction cross section by summing the total reaction probability over all partial waves, and the rate constant was averaged over the Boltzmann factor to obtain values from 10 to 100 K.

To compare the theoretical rate constants to the measured ones, a temperature-dependent electronic factor (*18*) was included to describe the fine-structure distribution of $OH(X^2\Pi)$ and the degeneracy of the electronic states of HNO and $N(^4S)$. Detailed descriptions of both the experimental and theoretical methods can be found in (*14*). The measured rate constants are in excellent agreement with the present theoretically determined values at all temperatures, as well as with other recent calculations (*10*–*12*) predicting a weak variation of the reaction rate between 50 and 500 K, with the exception of Ge *et al.* (*19*). Moreover, the good agreement between the J-shifted TIQM and all J TDQM results indicates the validity of the J-shifting model for this system. This is in contrast to a recent study of the O + OH → H + O_2 reaction (*20*) where the J-shifting approach led to substantial errors. The present experimental results are also in good agreement with a previous room-temperature study (*21*), although they neither support the pronounced negative temperature dependence nor the overall magnitude of the previously measured low-temperature rate constants (*9*, *22*). The discrepancy between the current and previous low-temperature experimental studies of reaction 1 may originate from several sources. Cryogenic cooling methods such as those used by Smith and co-workers (*9*, *22*) are potentially susceptible to interferences from heterogeneous processes. Moreover, the accurate determination of atomic concentrations in such systems is far from trivial.

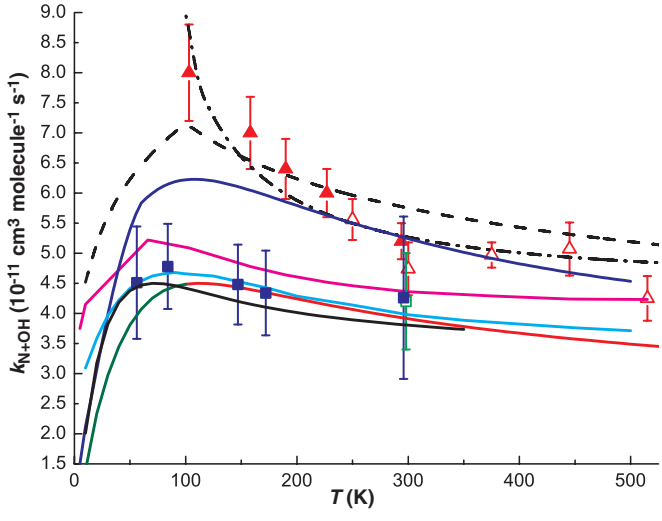

Fig. 3. Rate constants for the $N(^4S)$ + $OH(^2\Pi)$ reaction as a function of temperature. Experimental values: solid red triangles, Smith and Stewart (*9*); open red triangles, Howard and Smith (*22*); open green squares, Brune *et al.* (*21*); solid blue squares, this work. Theoretical values: pink line, Edvardsson *et al.* (*10*); light blue line, Jorfi *et al.* (*11*); red line, Li *et al.* (*12*); dark blue line, Ge *et al.* (*19*). This work: solid black line, TIQM J-shifting; green line, TDQM all J. Recommended values: dot-dashed line, Woodall *et al.* (*7*); dashed line, Wakelam *et al.* (*8*). Error bars on the present values indicate the combined statistical uncertainty at the level of a single standard deviation and an estimated 10% systematic uncertainty (see table S1).

Conversely, the present technique is hampered by neither of these issues (*14*).

The excellent agreement between theoretically and experimentally determined rate constants for reaction 1 presented here validates these methods and should permit the measurement of rate constants for a wide range of atom-radical reactions in the near future. It is envisaged that reactions of ground-state atomic nitrogen and oxygen with other small diatomic radicals (CN, CH, C_2) will be among the first to be investigated. Our results also bear on the discrepancies between observed N/N_2 abundance ratios and those predicted by current astrochemical models. Maret *et al*. (*6*) used parameters given by the Ohio State University astrochemical database (OSU 2005) (*23*) to obtain rate constants for reactions 1 and 2 in their chemical model of the B68 prestellar core. At 10 K, these parameters yield rate constants of 1.4×10^{-10} $cm^3\ s^{-1}$ and 2.3×10^{-10} $cm^3\ s^{-1}$ for reactions 1 and 2, respectively. The present results can be used to estimate a rate constant for reaction 1 of 2.5×10^{-11} $cm^3\ s^{-1}$ at 10 K. Similarly, from recent experimental (*5*) and theoretical studies (*24*, *25*) of reaction 2, we estimate a rate constant of 7×10^{-12} $cm^3\ s^{-1}$. With values 5 and 30 times smaller than those used in the model example (*6*), this gas-phase N_2 formation mechanism should be less important than previously thought.

References and Notes

1. E. Herbst, H.-H. Lee, D. A. Howe, T. J. Millar, *Mon. Not. R. Astron. Soc.* **268**, 335 (1994).
2. CRESU stands for Cinétique de Reaction en Ecoulement Supersonique Uniforme and was applied to the study of reactions between neutral species by Sims *et al*. (*26*).
3. C. Berteloite *et al*., *Phys. Rev. Lett.* **105**, 203201 (2010).
4. D. Carty, A. Goddard, S. P. K. Köhler, I. R. Sims, I. W. M. Smith, *J. Phys. Chem. A* **110**, 3101 (2006).
5. A. Bergeat, K. M. Hickson, N. Daugey, P. Caubet, M. Costes, *Phys. Chem. Chem. Phys.* **11**, 8149 (2009).
6. S. Maret, E. A. Bergin, C. J. Lada, *Nature* **442**, 425 (2006).
7. J. Woodall, M. Agúndez, A. J. Markwick-Kemper, T. J. Millar, *Astron. Astrophys.* **466**, 1197 (2007).
8. V. Wakelam *et al*., *Space Sci. Rev.* **156**, 13 (2010).
9. I. W. M. Smith, D. W. A. Stewart, *J. Chem. Soc. Faraday Trans.* **90**, 3221 (1994).
10. D. Edvardsson, C. F. Williams, D. C. Clary, *Chem. Phys. Lett.* **431**, 261 (2006).
11. M. Jorfi, P. Honvault, P. Halvick, *Chem. Phys. Lett.* **471**, 65 (2009).
12. A. Li, C. Xie, D. Xie, H. Guo, *J. Chem. Phys.* **134**, 194309 (2011).
13. J. Daranlot *et al*., *ChemPhysChem* **11**, 4002 (2010).
14. Materials and methods are detailed in the supporting material at *Science* Online.
15. P. Honvault, J.-M. Launay, in *Theory of Chemical Reaction Dynamics*, A. Lagana, G. Lendvay, Eds. (Kluwer, Dordrecht, Netherlands, 2004), pp. 187–215.
16. J. M. Bowman, *J. Phys. Chem.* **95**, 4960 (1991).
17. Z. Sun, H. Guo, D. H. Zhang, *J. Chem. Phys.* **132**, 084112 (2010).
18. M. M. Graff, A. F. J. Wagner, *J. Chem. Phys.* **92**, 2423 (1990).
19. M.-H. Ge, T.-S. Chu, K.-L. Han, *J. Theor. Comput. Chem.* **7**, 607 (2008).
20. F. Lique *et al*., *J. Chem. Phys.* **131**, 221104 (2009).
21. W. H. Brune, J. J. Schwab, J. G. Anderson, *J. Phys. Chem.* **87**, 4503 (1983).
22. M. J. Howard, I. W. M. Smith, *J. Chem. Soc. Faraday Trans. II* **77**, 997 (1981).
23. E. Herbst, Ohio State University Astrochemical Database (update OSU.2005); www.physics.ohio-state.edu/~eric/research_files/osu.2005.
24. M. Jorfi, P. Honvault, *J. Phys. Chem. A* **113**, 10648 (2009).
25. P. Gamallo, R. Martínez, R. Sayós, M. González, *J. Chem. Phys.* **132**, 144304 (2010).
26. I. R. Sims *et al*., *J. Chem. Phys.* **97**, 8798 (1992).

Acknowledgments: Our experimental work was supported by the Agence Nationale de la Recherche (grant ANR-JC08_311018), the Conseil Régional d'Aquitaine (grant 20091102002), and the European Union (grant PERG03-GA-2008-230805). Our theoretical work was supported by the Mésocentre de Calcul de Franche-Comté (M.J. and P.H.), the U.S. Department of Energy (H.G.) and the National Natural Science Foundation of China (grants 21133006, 91021010, and 20725312) (D.X.). The data described in this work can be obtained from the corresponding author on request.

Supporting Online Material

www.sciencemag.org/cgi/content/full/334/6062/1538/DC1
Materials and Methods
Table S1
References (*27*–*44*)

9 September 2011; accepted 19 October 2011
10.1126/science.1213789

Observing the Multiexciton State in Singlet Fission and Ensuing Ultrafast Multielectron Transfer

Wai-Lun Chan, Manuel Ligges, Askat Jailaubekov, Loren Kaake, Luis Miaja-Avila, X.-Y. Zhu*

Multiple exciton generation (MEG) refers to the creation of two or more electron-hole pairs from the absorption of one photon. Although MEG holds great promise, it has proven challenging to implement, and questions remain about the underlying photo-physical dynamics in nanocrystalline as well as molecular media. Using the model system of pentacene/fullerene bilayers and femtosecond nonlinear spectroscopies, we directly observed the multiexciton (ME) state ensuing from singlet fission (a molecular manifestation of MEG) in pentacene. The data suggest that the state exists in coherent superposition with the singlet populated by optical excitation. We also found that multiple electron transfer from the ME state to the fullerene occurs on a subpicosecond time scale, which is one order of magnitude faster than that from the triplet exciton state.

The absorption of one photon in most semiconductor materials creates one electron-hole pair, which may be separated to give electrical current in a photovoltaic device. The solar-to-electric power-conversion efficiency from such a device comprising a single semiconductor material is theoretically limited to ~31%. This value, referred to as the Shockley-Queisser (SQ) limit (*1*), comes about because any excess kinetic energy of electron-hole pairs excited by photons with energy above the bandgap is typically lost as waste heat. One viable approach to exceed the SQ limit is to use materials in which the excess energy from the absorption of one photon can create two or more electron-hole pairs in a process called multiple exciton generation (MEG), or carrier multiplication in inorganic semiconductors (*2*, *3*) and singlet fission (SF) in the more localized molecules (*4*). MEG has been observed in semiconductor nanocrystals (*5*–*8*) and single-walled carbon nanotubes (*9*) and has been predicted to occur efficiently in graphene (*10*). SF in organic molecules is also well established (*4*) and can approach quantum efficiencies as high as 200% (*11*).

Implementing MEG or SF in high-efficiency solar cells requires extraction of multiple electrons or holes from the light-harvesting material. This is challenging because in competition with charge extraction, there are a number of competing channels for the decay of multiple excitons. For example, enhanced Coulomb interaction (*12*) is believed to be responsible for high MEG yield in quantum-confined materials but also increases the efficiency of Auger recombination (the reverse of MEG). Charge-carrier extraction from multiple excitons has been demonstrated with the assistance of external bias voltage in photodiodes of single-walled carbon nanotubes (*9*), PbS nanocrystal thin films (*13*), and pentacene/C_{60} multilayers (*14*). Multiple charge transfer has also been reported for molecular electron acceptors anchored to semiconductor nanocrystals (*15*) and in semiconductor nanocrystal-sensitized electrochemical solar cells (*16*).

In the above demonstrations and in extensive ongoing efforts, the common strategy has been to extract charge carriers from the product of the MEG or SF process, that is, relaxed (band-edge) or localized multiple excitons. However, this approach may not be the best strategy to harvest carriers resulting from MEG. Theoretical studies of SF in molecular materials have shown that the process involves a multiexciton (ME) intermediate state, which is essentially a correlated triplet

Department of Chemistry and Biochemistry, University of Texas, Austin, TX 78712, USA.

*To whom correspondence should be addressed. E-mail: zhu@cm.utexas.edu